

Cold-atom shaping with MEMS scanning mirrors

ALAN BREGAZZI,^{1,*} PAUL JANIN,² SEAN DYER,¹ JAMES P. MCGILLIGAN,¹ OLIVER BURROW,¹ ID
ERLING RIIS,¹ DEEPAK UTTAMCHANDANI,² RALF BAUER,² ID AND PAUL F. GRIFFIN¹ ID

¹SUPA and Department of Physics, University of Strathclyde, G4 0NG, Scotland, UK

²Department of Electronic and Electrical Engineering, University of Strathclyde, Glasgow, G1 1XW, Scotland, UK

*Corresponding author: alan.bregazzi@strath.ac.uk

Received 9 September 2022; revised 28 October 2022; accepted 2 November 2022; posted 17 November 2022; published 16 December 2022

We demonstrate the integration of micro-electro-mechanical-systems (MEMS) scanning mirrors as active elements for the local optical pumping of ultra-cold atoms in a magneto-optical trap. A pair of MEMS mirrors steer a focused resonant beam through a cloud of trapped atoms shelved in the $F = 1$ ground-state of ^{87}Rb for spatially selective fluorescence of the atom cloud. Two-dimensional control is demonstrated by forming geometrical patterns along the imaging axis of the cold atom ensemble. Such control of the atomic ensemble with a microfabricated mirror pair could find applications in single atom selection, local optical pumping, and arbitrary cloud shaping. This approach has significant potential for miniaturization and in creating portable control systems for quantum optic experiments.

Published by Optica Publishing Group under the terms of the [Creative Commons Attribution 4.0 License](#). Further distribution of this work must maintain attribution to the author(s) and the published article's title, journal citation, and DOI.

<https://doi.org/10.1364/OL.475353>

Introduction. Over the last decades, significant effort has been directed toward reducing the size, weight, and power (SWaP) of cold-atom platforms, with recent research advances on compact vacuum cells [1–3], optical components for laser cooling [4–8], and magnetic trapping on “atom chips” [9,10]. As the maturity of cold atom platforms has advanced, work has more recently begun to focus on the surrounding technology for addressing and interrogating clouds of cold atoms. The drive here is toward portable and deployable cold atomic devices such as clocks and interferometers and cold atom quantum memories operating outside the laboratory environment [11–13].

One outstanding challenge for the miniaturization of atomic-based quantum sensors is that of dynamic manipulation of cold atom ensembles. Fine control of atom distributions by optical means is well established and used extensively throughout quantum optic experiments, from simple dipole traps [14] and optical tweezers [15], whose position is typically controlled by one-dimensional (1D) or two-dimensional (2D) acousto-optic modulator (AOM) devices, to more complex arbitrary atom arrays formed by spatial light modulators (SLMs) or digital micro-mirror devices (DMDs) [16,17]. These techniques also allow for shaping of time-averaged potentials, for example by scanning orthogonal AOM pairs [18,19] while simultaneously

providing a means to optically shutter the incident light. However, AOMs typically require RF signals in the 100 MHz range with 1 W of power, and need extended optical paths to allow spatial separation of diffracted orders. Application of SLMs and DMDs in cold-atom systems is continually advancing, yet these remain expensive, and also require similar optical footprints as AOM devices. With the goal of transitioning toward complete devices, these solutions for optical manipulation remain non-ideal.

Previous research has demonstrated the suitability of scanning micro-electro-mechanical-systems (MEMS) micro-mirrors as an alternative method of dynamically manipulating laser beams to enable addressing of neutral atom or ions with single-particle resolution. Work reported in the literature has used two orthogonally scanning MEMS mirrors to provide 2D control of beam position [20–22]. In contrast, in this Letter we demonstrate addressing of large ensembles of cold atoms direct from a magneto-optical trap (MOT). We present a proof-of-principle investigation of 2D time-averaged painted light potentials by selectively painting hyperfine-repumping light onto a cold atom ensemble using two silicon-on-insulator MEMS micro-mirrors. By independently controlling each mirror we locally excite and image fluorescence within the atom cloud in line, square, and circular geometries. We demonstrate a spatial resolution of $\sim 300\ \mu\text{m}$ and scan frequencies close to 90 kHz, with the mean local velocity of the addressing laser $>100\ \text{m/s}$, more than three orders of magnitude faster than the atomic motion. This technique is highly scalable, low SWaP, and offers the opportunity for simultaneous control of multiple wavelengths of light; typically more difficult to achieve with AOM control [23].

Experimental setup. As a basis for the proof-of-principle demonstration we use a grating magneto-optical trap (GMOT) formed by a $2\ \text{cm} \times 2\ \text{cm}$ three zone “tri” grating [4]. A commercial laser system (Muquans ILS) outputting fiber coupled light at 780 nm is used throughout as a source of trapping, imaging light, and main re-pump light. This allows for laser frequency tuning of $\approx 1\ \text{GHz}$ over the whole $^{87}\text{Rb}\ D_2$ line with an internal AOM for power control and an electro-optic modulator (EOM) to provide re-pump light during the trapping process. From the fiber we expand the beam to a $1/e^2$ radius of $\approx 2\ \text{cm}$, circularly polarize it with a quarter wave plate and align onto the grating. A simplified schematic of the experimental setup is shown in Fig. 1(a), highlighting the optical axis for cooling, MEMS addressing and imaging.

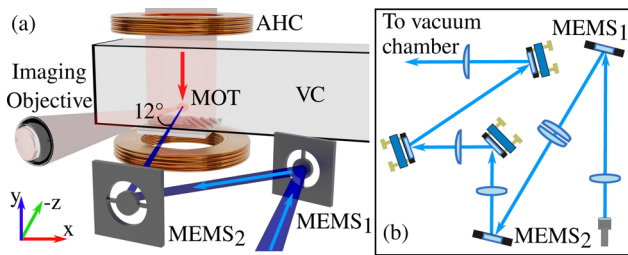


Fig. 1. (a) Simplified experimental setup. A single trap beam (red) is aligned onto a grating chip mounted externally to a vacuum cell (VC); also shown are the anti-Helmholtz trapping coils (AHC). The MEMS addressing beam (blue) is shown aligned into the MOT region with two orthogonally scanning MEMS mirrors: MEMS₁ scans the x axis while MEMS₂ scans the y axis. The imaging axis is shown rotated by 12° from the MEMS addressing axis. (b) Overview of full MEMS scanning system, showing the re-pump beam preparation and alignment using two MEMS scanners.

The experimental sequence is initiated by turning on a pair of anti-Helmholtz trapping coils producing a gradient field of ≈ 15 G/cm. The laser frequency is set to be $\Delta = 2\Gamma$ red detuned ($\Gamma/2\pi = 6.07$ MHz) from the $F = 2 \rightarrow F' = 3$ cycling transition, while re-pump is provided by the EOM, modulated at 6.57 GHz to produce sidebands on the carrier light with 5% of the total power. We load $\approx 2 \times 10^6$ atoms into the GMOT in 2 s before beginning a 10 ms initial red molasses cooling stage. During this initial cooling, the trapping coils are turned off and the carrier detuning is linearly ramped to -5Γ while simultaneously decreasing the beam intensity from $12I_{\text{sat}}$ to $3I_{\text{sat}}$, where the average $I_{\text{sat}} = 3.5$ mW/cm² over all polarizations is used [24]. We then perform a second shorter gray molasses cooling stage [25] where the laser frequency is jumped to 5Γ blue detuned from the $F = 2 \rightarrow F' = 2$ transition with the EOM frequency changed to 6.83 GHz to concurrently tune the re-pump frequency. The laser intensity is also raised to $12I_{\text{sat}}$ and linearly scanned back down to $3I_{\text{sat}}$ in 3 ms, resulting in an atomic temperature of ~ 50 μ K. This second molasses stage was utilized due to the higher atomic densities typical of gray molasses [26], giving higher signal-to-noise ratio in the resulting MEMS re-pump addressing images. In addition to this, gray molasses efficiently pumps the atoms into the dark $F = 1$ ground-state [26], helping to prepare them for the MEMS addressing stage. Once the atom cloud has been prepared in the $F = 1$ ground-state the main re-pump light derived from the EOM is turned off with an extinction of 65 dB to ensure that the only re-pump light incident on the atoms originates from the MEMS addressing. We then wait 1 ms with the cooling beam on to ensure as many atoms as possible are shelved in the $F = 1$ ground-state before turning the MEMS addressing beam on.

The MEMS addressing beam is derived from an extended cavity diode laser (ECDL) [27] locked via saturated absorption spectroscopy. The power level of this light is controlled using a single pass AOM that can be rapidly turned on and off. This light, now resonant with the D₂ $F = 1 \rightarrow F' = 2$ transition, is then fiber coupled and passed to the MEMS mirror scanning system.

The scanning system is based on a pair of MEMS scanners to steer the MEMS addressing beam in two dimensions onto the cold atom cloud. Each scan axis is driven near the respective mirror's resonance frequency, which for one of the mirrors can

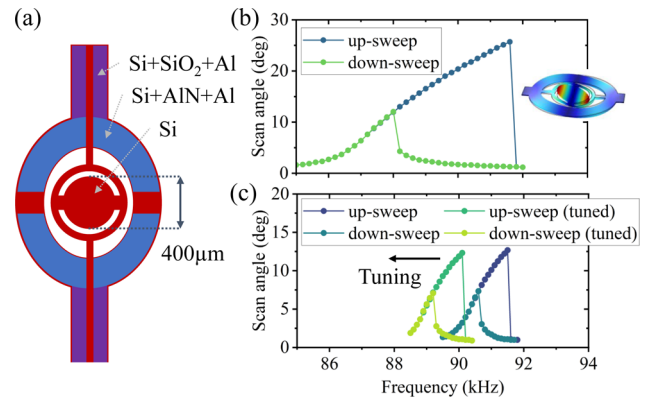


Fig. 2. MEMS mirror characteristics: (a) schematic of the used $400 \mu\text{m}$ diameter mirror; (b) frequency response for MEMS₁; (c) frequency response for tuning of MEMS₂.

be thermally tuned to create the desired scan profiles. The fiber-coupled laser beam is collimated into free space with a waist of 1 mm and focused to a point roughly 30 mm before the surface of the first MEMS scanner (MEMS₁) by a 150 mm focal length achromatic lens. The beam reflected from MEMS₁ is imaged onto MEMS₂ by a matched achromatic doublet pair with 100 mm focal length, ensuring that beam steering deflections originate from the same point on the optical axis. The MEMS are positioned to align their scan axes orthogonally. The scanner image is then relayed through a 30 mm focal length achromat followed by a 200 mm plano-convex lens, such that the final scanner image is placed in the object plane of the final focusing lens; creating a telecentric illumination. Furthermore, placing the scanner out of focus of the initial lens allows collimation of the beam before the final imaging lens, and focusing at the target, such that scanline focusing is decoupled from the beam focusing.

The scanners themselves are custom built resonant piezoelectric MEMS with $400 \mu\text{m}$ mirror aperture fabricated using a commercial multiuser process (MEMSCAP PiezoMUMPS) [28]. The scanner design is shown in Fig. 2(a). A dual frame allows for placement of four aluminum nitride piezoelectric actuators on the outer frame, coupling and magnifying its out of plane rotation motion to the mirror surface. The frequency response of both scanners was independently measured, with the characteristics of the first scanner shown in Fig. 2(b) and the second scanner in Fig. 2(c). In the following, both MEMS are actuated around the fundamental tilt resonance mode of the mechanical structure, rotating the mirror along the suspension beams connecting the mirror surface to the inner frame. The corresponding resonance frequency is around 90 kHz with a maximum optical scan angle of 25° and 12° using an offset sine-wave actuation with $40 V_{pp}$ and $20 V_{DC}$ offset [see Figs. 2(b) and 2(c)]. In both cases a hysteresis behavior of the frequency response is apparent, with nonlinearities leading to a higher movement scan angle being reachable when approaching the resonance peak from lower frequencies. For MEMS₁ this leads to the larger angular response in the frequency range between 88 and 92 kHz to only be reachable when starting the movement below 88 kHz, while for MEMS₂ the same behavior is present in the frequency range between 90.5 and 91.5 kHz.

In order to compensate for discrepancies in resonance frequencies between the two scanners resulting from variations

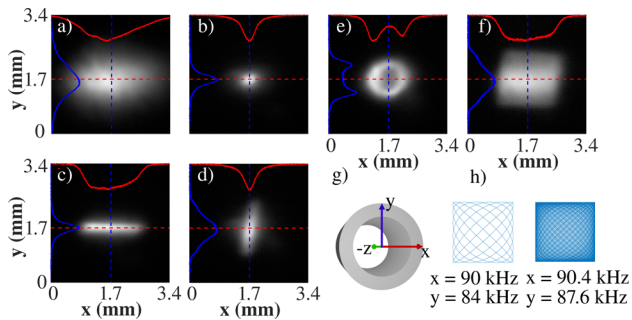


Fig. 3. (a) Images of atomic fluorescence for $\approx 2 \times 10^6$ atoms loaded into the standard GMOT. (b) Region of atom cloud illuminated by MEMS addressing beam with no MEMS scanning. (c) Horizontal MEMS mirror scan. (d) Vertical MEMS mirror scan. (e) Circular scan driving both MEMS with the same frequency and $\pi/2$ phase shift. (f) Square scan using both MEMS with Lissajous scanning. All images are individually normalized. (g) A pictorial representation of the 2D circular scan, projected into three dimensions, observed at 12° with respect to the MEMS addressing beam propagating along the z axis. The traces in (h) show the 2D scan profiles for the atomic fluorescence profile in (f), highlighting a general Lissajous scan profile for illustration next to the used profile.

and tolerances during the fabrication process, MEMS₂ can be tuned by localized heating of the device through three on-chip thermal actuators. This concept is described in detail in Ref. [28]. Through thermal tuning, the resonance frequency can be reduced by around 1.5 kHz, from 91.5 to 90 kHz, making actuation at 90 kHz possible with sufficient optical scan amplitude for synchronized scanning purposes.

Imaging of the atom cloud was performed by standard fluorescence detection on a charge-coupled device (CCD) camera with the imaging axis offset by 12° from the addressing axis due to optical access.

Results. An image of the whole atom cloud after optical molasses is shown in Fig. 3(a). This image was taken with the main experimental re-pump light, derived from the EOM, incident on the atoms and shows the extent of the atom cloud to be roughly 3 mm in the horizontal axis and 1.6 mm in the vertical axis. Fig. 3(b) shows an image of the atom cloud after extinguishing the main re-pump light and turning the MEMS addressing beam on with no MEMS mirror scanning present. When a Gaussian distribution is fitted to the vertical axis of the image in Fig. 3(b) a waist of $300 \mu\text{m}$ is calculated. This differs to measurements of the MEMS addressing beam giving a beam waist of $40 \mu\text{m}$. The apparent broadening is largely attributed to the relatively long exposure time of the fluorescence images of 1 ms and heating of atomic cloud during near-resonant imaging, resulting in the motion of atoms within this time window. These parameters were required to optimize signal-to-noise in our imaging system. This broadening of the resolution could be reduced by a higher-collection efficiency imaging or by absorption imaging.

By actuating each MEMS mirror individually we can create single line scans in the horizontal and vertical axes, as shown in Figs. 3(c) and 3(d), respectively. These narrow line potentials are again broadened with respect to the incident beam, giving waists of $260 \mu\text{m}$ for the horizontal scan and $380 \mu\text{m}$ for the vertical scan, with a scan length of 2 mm and 1.4 mm, respectively. The additional broadening of the vertically scanned beam is likely due to the imaging axis being rotated with respect to

the incident beam. When the 2D scan line is projected onto the three-dimensional (3D) MOT, the resulting distribution of bright atoms is a plane through the center of the MOT. When this plane is viewed at an angle with respect to the scanning beam some of the bright atoms from the back of the plane are projected onto the imaging plane.

Line profiles showing the intensity profiles through the center of the cloud are shown by the red and blue overlays in Figs. 3(a)–3(f). Local fluorescence within the atom cloud results from a combination of the local atomic density and the time-averaged beam intensity at each location along the scan axis. Due to the rotation of the mirrors around their fundamental tipping mode, the addressing beam spends more time interacting with atoms at the extremes of the scan. By contrast, however, there is a lower atomic density at the edges of the scans due to the MOT’s Gaussian profile. The combination of these effects in the ideal case leads to a flattened intensity profile around the center of the MOT with Gaussian edges originating from the Gaussian addressing beam as shown in Fig. 3(c). When scanning vertically as in Fig. 3(d) the intensity profile can be seen to diverge significantly from the ideal square case. This discrepancy between the horizontal and vertical scans is due to the characteristic “pancake” shape of GMOTs, where slightly larger axial trapping forces compared with radial trapping cause the MOT to be compressed in the vertical axis [24]. When the scan length is of the same order as the atom cloud’s dimension in that axis the larger variation in atomic density across the scan length causes this deviation in the scan profiles.

Next the mirrors were simultaneously driven around their respective resonance frequencies (87.6 kHz for MEMS₁ and 90.4 kHz for MEMS₂), producing a time-averaged square light potential within the cloud, shown in Fig. 3(f). This results from the Lissajous scan pattern with 1.97×10^5 crossover points per axis, generated by the precise frequency spacing between both base resonances. This concept is illustrated in Fig. 3(h) where simulations of the resulting scan profile are shown for two different scan frequencies. Line profiles through each axis of this image once again show a good approximation to a square profile in the horizontal axis with the vertical axis deviating significantly from the ideal square potential.

A circular scan, shown in Fig. 3(e), is generated when the resonance frequencies of both MEMS mirrors are identical, with a 90° phase shift between their movements. To achieve this the frequency tuning actuation of MEMS₂ was utilized, with a 7.5 V_{DC} tuning voltage applied to one of the thermal tuning actuators and 10 V_{DC} to the other two, while MEMS₁ was left at its original resonance. This led to a matched resonance frequency and therefore circular scan frequency of 90 kHz, with the scanning beams creating a trace for a ring potential. One requirement for optical ring potentials within BECs for interferometry is that the light potential is smooth across the whole profile of the ring. While Fig. 3(e) shows a clear imbalance in intensity of the left-hand side of the ring compared with the right-hand side, this effect is primarily due to the 12° rotation in the imaging axis with respect to the MEMS addressing beam. This rotation means the 3D hollow cylinder of bright atoms is projected into the imaging plane at an angle. The pixel counts measured by the CCD are proportional to both the atomic scattering rate and density of atoms, taking into account the 3D nature of the hollow cylinder of bright atoms. As highlighted in Fig. 3(g) one side of the image will be integrated over a higher density of atoms than the other, resulting in the intensity imbalance

observed in Fig. 3(e). Another contributor to this intensity imbalance is local variations in atomic density, visible in Fig. 3(a). Previous demonstrations of ring potentials have accounted for these local variations in density by modulating the light intensity as it is scanned with orthogonal AOMs [19]. Implementing some feedback on light intensity the 2D MEMS mirror scanner would also serve to create smoother potentials for use in portable quantum optic experiments, with required modulation frequencies of 90 kHz within easy reach of direct diode modulation schemes.

Conclusions. The work in this Letter represents an advance over previously reported work combining cold atoms and MEMS scanning or steering mirrors where addressing was limited to individual atoms or ions on discrete sites. We have demonstrated the first, to our knowledge, experimental system for shaping time-averaged light potentials in cold atom ensembles using MEMS mirrors. By independently driving two orthogonally scanning MEMS mirrors with resonance frequencies above 90 kHz we are able to form geometric patterns—line, circle, and filled-square profiles of bright fluorescing atoms within a larger dark atom. This technique further demonstrates the applicability of MEMS microfabrication techniques for replacing high SWaP laboratory-based equipment, building on previous research toward the miniaturization of cold atom experiments for the realization of truly portable cold atom sensors.

The wide bandwidth of available reflection coatings on the MEMS mirrors make this technique ideal for simultaneous control of multiple wavelengths of light. The technique could be extended to dynamic beam shuttering. More dynamic control of the scan amplitude and phase would make it possible to form more complex geometries opening the technique to more applications such as the storing of images for quantum information processing [29], selection of individual layers of optical lattices [30], generation of arbitrary geometry matterwave circuits [31], and all-optical adaptable atomtronics [32]

Funding. Defence Science and Technology Laboratory; Royal Academy of Engineering (RF/202021/20/343, RF1516/15/8); Engineering and Physical Sciences Research Council (EP/S032606/1, EP/T001046/1).

Acknowledgments. We thank Dr Aidan Arnold for stimulating conversations. A.B. was supported by a PhD studentship from the Defence Science and Technology Laboratory (DSTL) and P.J. was supported by a studentship from the National Physical Laboratory (NPL).

Disclosures. The authors declare no conflicts of interest.

Data availability. Data underlying the results presented in this paper are available in Ref. [33].

REFERENCES

- J. P. McGilligan, K. R. Moore, A. Dellis, G. D. Martinez, E. de Clercq, P. F. Griffin, A. S. Arnold, E. Riis, R. Boudot, and J. Kitching, *Appl. Phys. Lett.* **117**, 054001 (2020).
- R. Boudot, J. P. McGilligan, K. R. Moore, V. Maurice, G. D. Martinez, A. Hansen, E. de Clercq, and J. Kitching, *Sci. Rep.* **10**, 16590 (2020).
- A. Bregazzi, P. F. Griffin, A. S. Arnold, D. P. Burt, G. Martinez, R. Boudot, J. Kitching, E. Riis, and J. P. McGilligan, *Appl. Phys. Lett.* **119**, 184002 (2021).
- C. C. Nshii, M. Vangeleyn, J. P. Cotter, P. F. Griffin, E. A. Hinds, C. N. Ironside, P. See, A. G. Sinclair, E. Riis, and A. S. Arnold, *Nat. Nanotechnol.* **8**, 321 (2013).
- N. Chauhan, D. Bose, M. Puckett, R. Moreira, K. Nelson, and D. J. Blumenthal, in *Conference on Lasers and Electro-Optics*, (OSA, 2019).
- A. Sitaram, P. K. Elgee, G. K. Campbell, N. N. Klimov, S. Eckel, and D. S. Barker, *Rev. Sci. Instrum.* **91**, 103202 (2020).
- L. Zhu, X. Liu, B. Sain, M. Wang, C. Schlickriede, Y. Tang, J. Deng, K. Li, J. Yang, M. Holynski, S. Zhang, T. Zentgraf, K. Bongs, Y.-H. Lien, and G. Li, *Sci. Adv.* **6**, eabb6667 (2020).
- W. R. McGehee, W. Zhu, D. S. Barker, D. Westly, A. Yulaev, N. Klimov, A. Agrawal, S. Eckel, V. Aksyuk, and J. J. McClelland, *New J. Phys.* **23**, 013021 (2021).
- J. Reichel, W. Hänsel, and T. W. Hänsch, *Phys. Rev. Lett.* **83**, 3398 (1999).
- R. Folman, P. Kruger, J. Schmiedmayer, J. Denschlag, and C. Henkel, "Microscopic atom optics: from wires to an atom chip," *arXiv arXiv:0805.2613* (2008).
- T. Müller, M. Gilowski, M. Zaiser, P. Berg, C. Schubert, T. Wendrich, W. Ertmer, and E. M. Rasel, *Eur. Phys. J. D* **53**, 273 (2009).
- F. Sorrentino, K. Bongs, and P. Bouyer, *et al.*, *Microgravity Sci. Technol.* **22**, 551 (2010).
- T. Chanelière, D. N. Matsukevich, S. D. Jenkins, S.-Y. Lan, T. A. B. Kennedy, and A. Kuzmich, *Nature* **438**, 833 (2005).
- R. Grimm, M. Weidemüller, and Y. B. Ovchinnikov, *Advances In Atomic, Molecular, and Optical Physics* (Elsevier, 2000), pp. 95–170.
- D. Barredo, S. de Léséleuc, V. Lienhard, T. Lahaye, and A. Browaeys, *Science* **354**, 1021 (2016).
- F. Nogrette, H. Labuhn, S. Ravets, D. Barredo, L. Béguin, A. Vernier, T. Lahaye, and A. Browaeys, *Phys. Rev. X* **4**, 021034 (2014).
- D. Stuart and A. Kuhn, *New J. Phys.* **20**, 023013 (2018).
- K. Henderson, C. Ryu, C. MacCormick, and M. G. Boshier, *New J. Phys.* **11**, 043030 (2009).
- T. A. Bell, J. A. P. Glidden, L. Humbert, M. W. J. Bromley, S. A. Haine, M. J. Davis, T. W. Neely, M. A. Baker, and H. Rubinsztein-Dunlop, *New J. Phys.* **18**, 089501 (2016).
- C. Knoernschild, X. L. Zhang, L. Isenhower, A. T. Gill, F. P. Lu, M. Saffman, and J. Kim, *Appl. Phys. Lett.* **97**, 134101 (2010).
- S. Crain, E. Mount, S. Baek, and J. Kim, *Appl. Phys. Lett.* **105**, 181115 (2014).
- Y. Wang, S. Crain, C. Fang, B. Zhang, S. Huang, Q. Liang, P. H. Leung, K. R. Brown, and J. Kim, *Phys. Rev. Lett.* **125**, 150505 (2020).
- S. Kim, R. R. Mcleod, M. Saffman, and K. H. Wagner, *Appl. Opt.* **47**, 1816 (2008).
- J. P. McGilligan, P. F. Griffin, E. Riis, and A. S. Arnold, *Opt. Express* **23**, 8948 (2015).
- D. S. Barker, E. B. Norrgard, N. N. Klimov, J. A. Fedchak, J. Scherschligt, and S. Eckel, *Opt. Express* **30**, 9959 (2022).
- S. Rosi, A. Burchianti, S. Conclave, D. S. Naik, G. Roati, C. Fort, and F. Minardi, *Sci. Rep.* **8**, 1301 (2018).
- A. S. Arnold, J. S. Wilson, and M. G. Boshier, *Rev. Sci. Instrum.* **69**, 1236 (1998).
- P. Janin, D. Uttamchandani, and R. Bauer, *J. Microelectromech. Syst.* **31**, 977 (2022).
- M. Shuker, O. Firstenberg, R. Pugatch, A. Ron, and N. Davidson, *Phys. Rev. Lett.* **100**, 223601 (2008).
- B. Peaudecerf, M. Andia, M. Brown, E. Haller, and S. Kuhr, *New J. Phys.* **21**, 013020 (2019).
- C. Ryu and M. G. Boshier, *New J. Phys.* **17**, 092002 (2015).
- Y. B. Ovchinnikov, *Appl. Phys. Lett.* **120**, 010502 (2022).
- A. Bregazzi, P. Janin, S. Dyer, J. P. McGilligan, O. Burrow, E. Riis, D. Uttamchandani, R. Bauer, and P. Griffin, "Data for: "Cold-atom shaping with MEMS scanning mirrors"" University of Strathclyde (2022), <https://doi.org/10.15129/4f23fe3b-e52c-43fd-8206-edc5806b2e50>.